



## Research Article

# Optimizing the microstructures and mechanical properties of Al-Cu-based alloys with large solidification intervals by coupling travelling magnetic fields with sequential solidification

Lei Luo<sup>a</sup>, Liangshun Luo<sup>a,\*</sup>, Robert O. Ritchie<sup>b</sup>, Yanqing Su<sup>a,\*</sup>, Binbin Wang<sup>a</sup>, Liang Wang<sup>a</sup>, Ruirun Chen<sup>a</sup>, Jingjie Guo<sup>a</sup>, Hengzhi Fu<sup>a</sup>

<sup>a</sup> National Key Laboratory for Precision Hot Processing of Metals, School of Materials Science & Engineering, Harbin Institute of Technology, Harbin 150001, China

<sup>b</sup> Department of Materials Science and Engineering, University of California, Berkeley, CA 94720, USA

## ARTICLE INFO

## Article history:

Received 23 March 2020

Received in revised form 27 April 2020

Accepted 24 May 2020

Available online 9 July 2020

## Keywords:

Large solidification intervals

Travelling magnetic fields

Sequential solidification

Mushy zones

Al-Cu-based alloys

## ABSTRACT

Alloys with large solidification intervals are prone to issues from the disordered growth and defect formation; accordingly, finding ways to effectively optimize the microstructure, further to improve the mechanical properties is of great importance. To this end, we couple travelling magnetic fields with sequential solidification to continuously regulate the mushy zones of Al-Cu-based alloys with large solidification intervals. Moreover, we combine experiments with simulations to comprehensively analyze the mechanisms on the optimization of microstructure and properties. Our results indicate that only downward travelling magnetic fields coupled with sequential solidification can obtain the refined and uniform microstructure, and promote the growth of matrix phase  $\alpha$ -Al along the direction of temperature gradient. Additionally, the secondary dendrites and precipitates are reduced, while the solute partition coefficient and solute solid-solubility are raised. Ultimately, downward travelling magnetic fields can increase the ultimate tensile strength, yield strength, elongation and hardness from 196.2 MPa, 101.2 MPa, 14.5 % and 85.1 kg mm<sup>-2</sup> without travelling magnetic fields to 224.1 MPa, 114.5 MPa, 17.1 % and 102.1 kg mm<sup>-2</sup>, and improve the ductility of alloys. However, upward travelling magnetic fields have the adverse effects on microstructural evolution, and lead to a reduction in the performance and ductility. Our findings demonstrate that long-range directional circular flows generated by travelling magnetic fields directionally alter the transformation and redistribution of solutes and temperature, which finally influences the solidification behavior and performance. Overall, our research present not only an innovative method to optimize the microstructures and mechanical properties for alloys with large solidification intervals, but also a detailed mechanism of travelling magnetic fields on this optimization during the sequential solidification.

© 2020 Published by Elsevier Ltd on behalf of The editorial office of Journal of Materials Science & Technology.

## 1. Introduction

Typically, large solidification intervals, *i.e.*, the difference in temperature between the liquidus and the solidus, in alloys such as Al-Cu, Al-Si, Sn-Bi and Pb-Sn, act to reduce the critical velocity for the steady growth of the flat solid-liquid interface during the solidification, which can result in the instability of the interface, in turn to form cellular and dendritic crystals [1–4]. It is widely believed that compositional undercooling occurs in the mushy zones more

readily due to the solute enrichment, so that deflected and disordered growth of the primary dendrites ensues, together with the prolific formation of secondary dendrites [5,6]. As a result, the feeding channels between the dendrites in the mushy zones become blocked, which obstructs the melt flows and increases the formation of shrinkage, pores and segregation defects [7–9]. Accordingly, the microstructural evolution during the solidification of alloys with large solidification intervals may largely increase the generation and quantity of defects [10–13], which naturally plays a negative role in the mechanical performance of the alloys [14,15]. Consequently, there is a persistent need to find ways to optimize the microstructure of as-cast alloys with large solidification intervals, to eliminate the defects and to improve mechanical

\* Corresponding authors.

E-mail addresses: [luoliangshunhit@163.com](mailto:luoliangshunhit@163.com) (L. Luo), [suqhit@163.com](mailto:suqhit@163.com) (Y. Su).

properties. At present, several methods have been proposed to achieve these goals. These approaches include primarily the refinement in the grain size and primary dendrite arm spacing (PDAS) of the as-cast microstructure [16] by adding the refiners [17], regulating the alloy melt [18,19], increasing the cooling rate [20,21], and performing the mechanical or electromagnetic stirring [22–24] and ultrasonic treatments [25]. By contrast, travelling magnetic fields (TMF) are especially attractive as they are non-contacting and pollution-free [26]. Moreover, during the solidification, buoyancy, Marangoni forces and the Lorentz forces induced by TMF will generate various directional circular flows rather than natural convection in the alloys melt, which can effectively control the heat and mass transport [27,28]. Several authors [29,30] have suggested that TMF processing can crush and break the secondary dendrite arms, additionally transfer the shredded fragments to the high-temperature melt zone or the undercooled liquid region for re-melting and re-nucleation. It has also been claimed that the redistribution of solute and temperature at the solidification front [31,32] produced by TMF can also change microstructural evolution in the alloys [33,34]. In short, TMF processing has the capability to refine and homogenize the microstructure of as-cast alloys, and further to reduce the generation of defects during the solidification process. Nevertheless, the specific microstructural improvement process for alloys with large solidification intervals are rare. Specifically, the studies on changes of solidification behavior and mechanical performance induced by TMF are unclear and incomplete; moreover, the mechanisms of TMF on improving as-cast microstructures remain systematically unexplained.

In light of this, in the current work we implement a coupling of TMF with sequential solidification, *i.e.*, a vertical upward unidirectional ordered solidification, to improve the microstructure and mechanical properties of Al-Cu-based alloys with large solidification intervals by continuously regulating the mushy zones. We additionally conduct a comprehensive study, by a combination of experiments and simulations, on the effects of TMF on variations of microstructure and performance by the sequential solidification. We propose three hypothetical mechanisms from the perspective of alloy melt flows, mass transfer, heat transfer, thermodynamics and mechanical forces, to determine the most reasonable mechanism. Our objective is to present an effective approach for the improvement of microstructure and mechanical performance of alloys with large solidification intervals, and to discern the most plausible explanation for the positive changes in solidification behavior induced by travelling magnetic fields.

## 2. Methods

### 2.1. Material preparation

A self-designed sequential solidification equipment coupled with TMF was used for the preparation of samples, as shown in Fig. 1a. Here, we define “Up-TMF”, “Down-TMF” and “No-TMF” as the solidification process with upward axial magnetic field force, with downward axial magnetic field force and without TMF respectively. In addition, sequential solidification was realized by rapidly cooling the bottom of alloy melt as shown in Fig. 1a. Considering the strong spatial and temporal dependence of TMF [31], we moved the alloy melt downward for 30 mm to keep the mushy zone in an effective region of the magnetic force before the solidification process started. Moreover, to achieve the coupling of TMF and sequential solidification, we moved the alloy melt downward by a constant velocity  $v_d = 150 \mu\text{m/s}$  to maintain the mushy zones in a stable position, which was given by:

$$v_d = v_c / G_T, \quad (1)$$

**Table 1**

Related characteristics of the TMF generator and the parameters used in the calculations of TMF and flow fields [35,36].

Parameters	Symbol	Value
TMF inner diameter	$D_i$ , mm	40
TMF outer diameter	$D_o$ , mm	120
Number of windings	$n$	330
Current frequency	$f$ , Hz	50
Phase sequence	–	Down-TMF: 0, $2\pi/3$ , $4\pi/3$ ; Up-TMF: $4\pi/3$ , $2\pi/3$ , 0
Maximum electric current	$I_0$ , A	24
Effective electric current	$I_e$ , A	17
Temperature gradient	$G_T$ , K mm <sup>-1</sup>	2
Cooling rate of alloys	$v_c$ , K s <sup>-1</sup>	0.3
Thermal Conductivity	$C_T$ , W mK <sup>-1</sup>	236
Magnetic permeability	$\mu_{Al}$ , H m <sup>-1</sup>	1
Viscosity coefficient	$\eta$ , Pa·s	0.00125
Electrical conductance	$\sigma$ , S m <sup>-1</sup>	35.3e+6
Latent heat	$L_m$ , kJ kg <sup>-1</sup>	396.1

**Table 2**

Preparation process of different samples and actual chemical compositions measured by XPS.

No.	Al, wt. %	Cu, wt. %	$I_e$ , A	TMF	$v_d$ , $\mu\text{m}\cdot\text{s}^{-1}$
1	Bal	4.99	17	Up-TMF	150
2	Bal	5.00	0	No-TMF	150
3	Bal	4.99	17	Down-TMF	150

Where  $G_T$  is the temperature gradient and  $v_c$  denotes the cooling rate of alloy melt, the values of which were the average of multiple experimental measurements. Besides, the related experimental and simulated parameters are shown in Table 1 [35,36]. Al-5 wt.%Cu alloys were used as model alloys in this study and prepared by using raw materials of pure aluminum (with high purity as 99.99 wt.%) and an Al-50 wt.%Cu master alloy. Each sample was melted at 1023 K in a resistance furnace and degassed with high-purity argon. After holding for 15 min., the alloy melt was poured into a corundum tube with 10 mm in diameter and 180 mm in length. The corundum tube was preheated in the tube furnace at 1023 K (Fig. 1a), where the sequential solidification process, with or without TMF, was carried out. The preparation process and chemical composition for samples are listed in Table 2.

### 2.2. Measurement and analysis methods

As shown in Fig. 1b, we selected a location between 70 and 130 mm from the bottom to the top of the castings along the growth direction, for the purpose of achieving the relatively stable directional microstructure of samples. We cut the selected samples in half evenly along the longitudinal direction, and analyzed their microstructure in the transverse and the longitudinal sections by using the scanning electron microscopy (SEM, Quanta 200FEG, FEI, USA) and three-dimensional computed tomography (3D-CT, Xradia 520 Versa, Zeiss, USA). In addition, energy dispersive spectroscopy (EDS, Quanta 200FEG, FEI, USA), X-ray diffraction (XRD, Empyrean, Panalytical, NL) and X-ray photoelectron spectroscopy (XPS, ESCALAB 250Xi, ThermoFisher, USA) were used together to determine the chemical composition of the precipitation phases in the microstructure. Crystal orientation, the volume fraction of the precipitates and the size of the dendritic crystals were measured using electron back-scattered diffraction (EBSD, Quanta 200FEG, FEI, USA). It is worth mentioning that the functions of SEM, EDS and EBSD are implemented on the same instrument. The measurements of tensile strength were performed at room temperature with a strain rate of  $10^{-3} \text{ s}^{-1}$  by universal testing machine (Instron5569, Instron, USA), and the tensile axis was paralleled to the growth direction of samples. The tensile tests were repeated three times

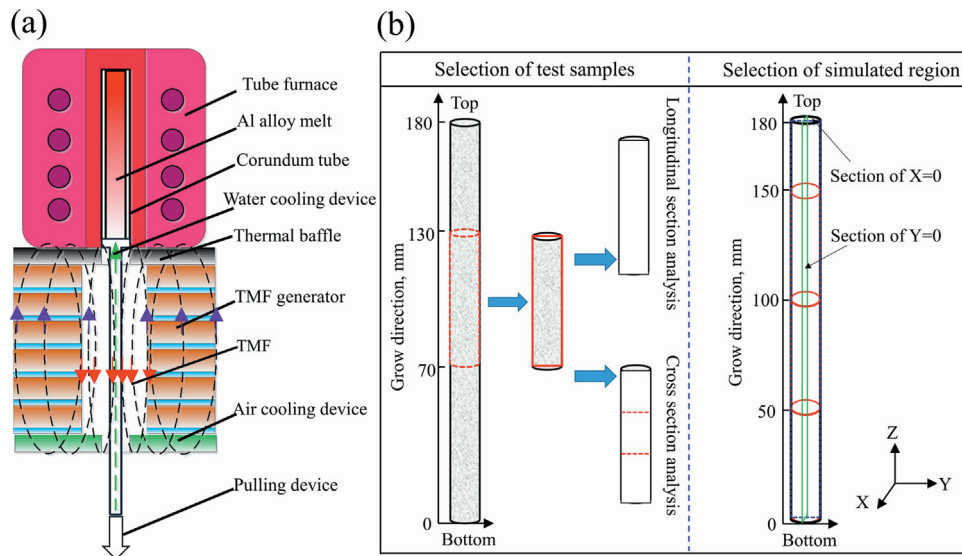


**Fig. 1.** Schematic diagrams of experiment and the selection of samples. (a) Equipment for the coupling of TMF with sequential solidification. (b) The selection of experimental samples and simulated models.

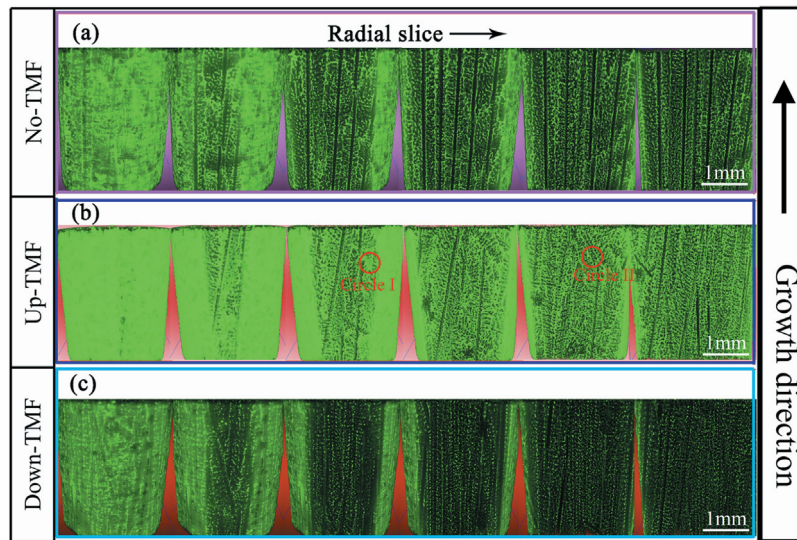


**Fig. 2.** Images of each slice along the radial direction taken by 3D-CT. Higher brightness in the images indicate the regions with higher content of Cu. With respect to microstructure, the green represents the Cu-containing precipitates, while the black within green represents the primary dendritic  $\alpha$ -Al. Circle I in (b) indicates the accumulation of Cu. Circle II in (b) indicates the deflection of the primary  $\alpha$ -Al dendrites.

to take the average value, of which the standard deviation was approximately 5%. Micro-hardness were measured by a hardness tester (HVS-1000A, Laizhou Huayin, CHN) with a 500 g load and a dwell time of 10 s. The average value of 10 times measurements was taken, of which the standard deviation was about 5%. The strength of the magnetic fields used in the experiments were measured by using a tesla-meter (HT201A, Shanghai Hengtong, CHN).

### 2.3. Simulations and calculations

Statistical analysis of the PDAS were performed by the Image-Pro software (Media Cybernetics, Inc., USA). Alloy phase diagrams were calculated by the Pandat software (CompuTherm LLC, USA). The magnetic fields and magnetic force density were simulated by using the Ansoft-Maxwell software (ANSYS Inc., USA). In addition, Ansoft-CFX software (ANSYS Inc., USA) was utilized to emulate the flow fields induced by TMF during the sequential solidification. Related parameters applied in the simulations are shown in Table 1.

In the simulations of magnetic fields, the following assumptions were made: (i) the permittivity, permeability and material conductivity involved in the calculations were assumed to be constant and regardless of the influence of temperature; (ii) each set of coils was considered as a unit, and the magnetic flux leakage between each two winds were neglected; (iii) the refractories attached to the TMF generator and the insulation materials in the experiments were modeled as regions of vacuum, because of their low permeability and non-conductivity; (iv) the heating of the melt caused by TMF were not considered in the simulations. Analogously, in the calculations of the melt flow fields, the following assumptions were made: (i) the initial mushy zone was simplified as the  $T_m = 821$  K isothermal region at 30–35 mm from the bottom of the alloy casting along the growth direction; (ii) the temperatures in regions below 30 mm were set as 820 K, while the regions above 35 mm were set as 1023 K to more clearly distinguish the evolution of the mushy zones; (iii) the corresponding temperatures in the melt at the original state were assumed to be stable; (iv) the magnetic forces were

assumed to be only applied to the melt with temperatures above, or equal to,  $T_m$ .

### 3. Results

It is well known that the prominent phases in Al-5 wt.%Cu alloys are mainly the Al-Cu precipitated phases and the matrix phase  $\alpha$ -Al dendrites [37–39], so we can separately analyze the evolution of precipitates and  $\alpha$ -Al. Additionally, according to the results in many literatures [40,41], we can determine that the matrix phase  $\alpha$ -Al dendrites originating from different nuclei embryo and growing along the direction of temperature gradient can be considered as the primary dendrites, which are also the focus of our research.

#### 3.1. Evolution of precipitates and variation of Cu solid solubility in matrix $\alpha$ -Al phase

The effects of TMF on the evolution of the precipitates occur primarily with respect to its distribution, content and transformation. Accordingly, we used the 3D-CT to analyze the three-dimensional microstructure of the samples, and processed the images to enhance the brightness of the regions with higher Cu content. Results shown in Fig. 2 can confirm that when TMF is not applied, the primary  $\alpha$ -Al dendrites mainly grow in the direction of temperature gradient (Fig. 2a); additionally, relatively coarse precipitates containing large amounts of Cu will primarily aggregate along the primary dendritic  $\alpha$ -Al boundaries. In addition, Up-TMF can cause the growth directions of the primary  $\alpha$ -Al dendrites to be deflected, and promote the substantial generation of secondary  $\alpha$ -Al dendrites (see Circle II in Fig. 2b). In this case, the high Cu-containing precipitates (see Circle I in Fig. 2b) will distribute largely at the front of the  $\alpha$ -Al primary dendrites growing along the direction of temperature gradient. In contrast, Down-TMF can effectively eliminate the formation of high Cu-containing precipitates, resulting in the refinement and uniform distribution of the remaining granular precipitates (Fig. 2c). In addition, we selected the central region of the samples and separated the three-dimensional morphology of the precipitated phases as shown in Fig. 3. It can be obtained that without TMF, the volume fraction of the precipitated phases is 7.56 %; which are mainly distributed along the direction of the temperature gradient, accompanied by the radial aggregation. It also can be observed that the addition of Up-TMF greatly increase the content of the precipitated phases (10.53 %) along the radial and longitudinal directions, resulted from the more severe enrichment of solute and the redistribution of temperature in front of primary phase  $\alpha$ -Al growing along the direction of temperature gradient. Conversely, with the application of the Down-TMF, the  $\alpha$ -Al can grow along the direction of the temperature gradient without hindrance. In this case, the volume fraction of precipitated phase decrease to 5.41 %, which are refined and uniformly distributed at the grain boundaries of the primary  $\alpha$ -Al phase.

Similarly, we analyzed the composition and content of precipitates in the microstructures with different TMF processes as shown in Fig. 4. Combining the results in Fig. 4c and Table 2, it is apparent that compared to the volume fraction of  $\text{Al}_2\text{Cu}$  in No-TMF processing (26.1 %), it can be decreased to 12.3 % with Down-TMF, whereas it will significantly be increased to 40.2 % with Up-TMF. There are large numbers of precipitates, including the stable  $\text{Al}_2\text{Cu}$  phase and the metastable  $\text{AlCu}_3$  and  $\text{AlCu}$  phases, appearing in both the transverse and longitudinal sections of the samples solidified with No-TMF and Up-TMF processing (Fig. 4a and b). However, with Down-TMF processing, the diffraction peaks of precipitates including the stable  $\text{Al}_2\text{Cu}$  phase and the metastable  $\text{AlCu}_3$  and  $\text{AlCu}$  phases are decreased relatively in both the transverse and longitudinal sections of the samples.

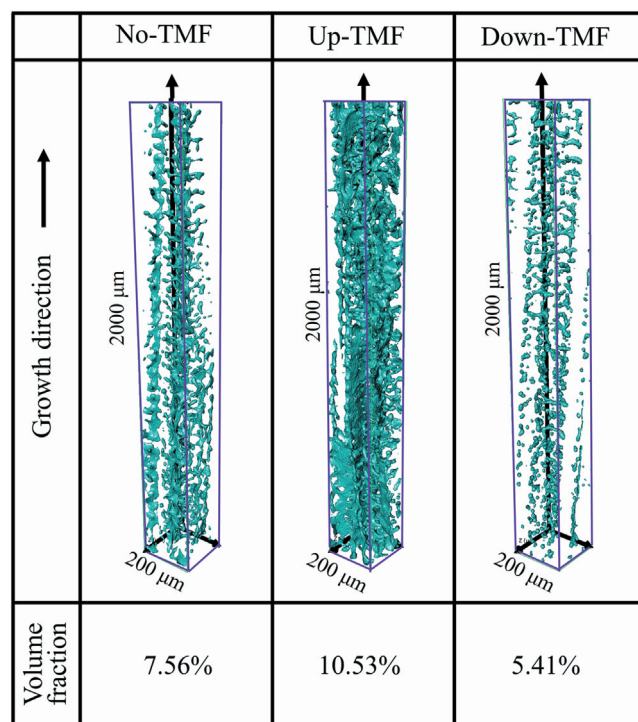


Fig. 3. Three-dimensional morphology of the precipitated phases taken by 3D-CT.

Table 3

Related results of the crystal structural evolution on the  $(200)_{\text{Al}}$  and  $(111)_{\text{Al}}$  crystal planes derived from the XRD data.

	Crystal face index	Samples		
		No-TMF	Up-TMF	Down-TMF
$(200)_{\text{Al}}$	$\theta$ , degree	44.781	44.779	45.040
	$a$ , nm	0.40444	0.40446	0.40222
	$S_{\text{max}}$ , at. %	0.6019	0.5555	5.7407
$(111)_{\text{Al}}$	$\theta$ , degree	38.555	38.555	38.817
	$a$ , nm	0.40410	0.40412	0.40149
	$S_{\text{max}}$ , at. %	1.3889	1.3426	7.4306

In order to study the reasons for the variations in precipitates and the distribution of the Cu atoms, we focused on the solid solubility  $S_{\text{max}}$  of Cu in the matrix  $\alpha$ -Al phase. To this end, we additionally analyzed the evolution of the precipitated phases via theoretical calculations of crystal structure measured by the XRD data in the transverse sections. First, we calculated the lattice constant  $a$  of the  $\alpha$ -Al, from Bragg's law [42] and the Scherrer formulas [43], in terms of the Miller indices  $H'$ ,  $K'$ ,  $L'$ , the x-ray wavelength  $\lambda = 0.154056$  nm, and the Bragg angle  $\theta$ , viz:

$$a = \frac{\lambda (H'^2 + K'^2 + L'^2)^{1/2}}{2 \sin \theta}. \quad (2)$$

The calculated results on the  $(200)_{\text{Al}}$  and  $(111)_{\text{Al}}$  crystal planes of  $\alpha$ -Al are presented in Table 3. Compared to No-TMF processing, Up-TMF processing always lead to an increase of the lattice constant  $a$  of the  $\alpha$ -Al grains on both the  $(200)_{\text{Al}}$  plane and the  $(111)_{\text{Al}}$  plane. On the contrary, with Down-TMF processing, the lattice constants of grains on each crystal plane are reduced. These changes in the lattice constant are closely related to the solid solubility  $S_{\text{max}}$  of Cu in the matrix  $\alpha$ -Al phase. Accordingly, we estimated the solid solubility  $S_{\text{max}}$  of Cu in the  $\alpha$ -Al phase matrix from the Vegard relationship [44]:

$$(1 - S_{\text{max}})a_0 + S_{\text{max}}a_1 = a, \quad (3)$$

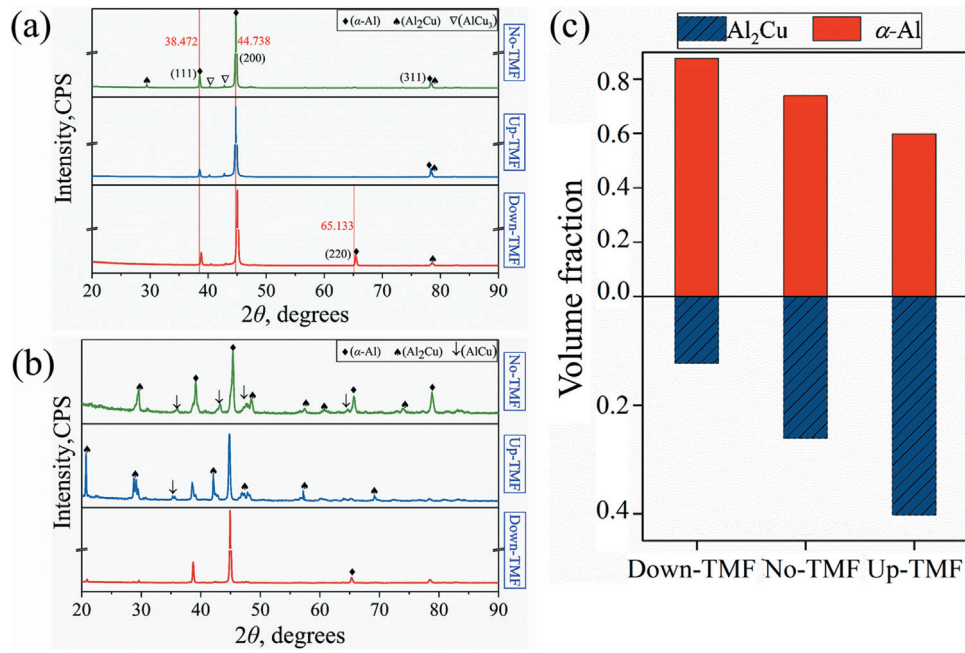


**Fig. 4.** The composition and content of precipitation phases. XRD maps of the (a) transverse and (b) longitudinal sections of the solidified samples. (c) The content statistics for the matrix phase  $\alpha$ -Al and precipitation phase  $\text{Al}_2\text{Cu}$ , as measured by EBSD.

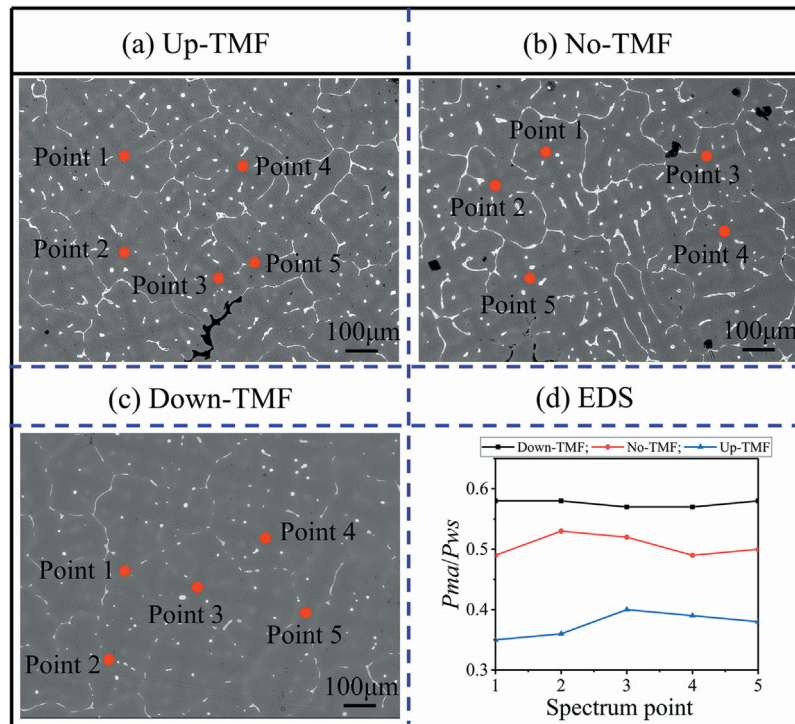


**Fig. 5.** Microstructural energy spectrum analysis measured in cross-sections of different samples. The red circles in (a), (b) and (c) represent the energy spectrum points. (d) The variation in  $P_{ma}$ ,  $P_{ws}$  and  $P_{ma}/P_{ws}$ , the corresponding values of each energy spectrum test point, which represent the concentration of Cu in the matrix, the concentration of Cu in the whole section and the relative solubility ratio, respectively.

where  $a_0$ ,  $a_1$  and  $a$  are respectively the lattice constant of the pure solvent element (Al), the solute element (Cu) and the matrix phase  $\alpha$ -Al. As Al and Cu are both the face-centered cubic with respective atomic radii of 0.1431 nm and 0.1278 nm, their lattice constants are 0.4047 nm and 0.3615 nm, respectively. Consequently, their solid solubility can be calculated from Eq. 3. Results listed in Table 3 can clearly demonstrate that compared to the processing without TMF (with a maximum  $S_{max}$  of 1.38 at.%), Down-TMF processing (with

a maximum  $S_{max}$  of 7.43 at.%) can substantially improve the solid solubility  $S_{max}$  of Cu in  $\alpha$ -Al, whereas Up-TMF processing (with a maximum  $S_{max}$  of 1.34 at.%) causes a slight decrease. In addition, we measured the distribution of Cu element in the microstructure by using EDS examination of the transverse section. To avoid errors caused by the segregation of Cu along the direction of temperature gradient, we measured the concentration of Cu in the  $\alpha$ -Al matrix ( $P_{ma}$ ) and in the whole section ( $P_{ws}$ ), as shown in Fig. 5

**Table 4**

EDS results for Cu element in the whole section<sup>a</sup> and at each point<sup>b</sup> (<sup>a</sup> “Whole section” refers to the weight percent of Cu in all areas of the microstructural images. <sup>b</sup> “Point” refers to the weight percent of Cu at each energy spectrum test point in the matrix phase  $\alpha$ -Al.).

Processing	Cu wt.%					
	Whole section	Point 1	Point 2	Point 3	Point 4	Point 5
Down-TMF	4.95	2.87	2.87	2.81	2.80	2.86
No-TMF	4.97	2.43	2.66	2.60	2.46	2.47
Up-TMF	4.97	1.75	1.81	2.01	1.92	1.87

and Table 4. Wherein, the  $P_{ma}$  of each samples was obtained by averaging the data of the five energy spectrum points. While,  $P_{ws}$  of each samples was obtained by surface scanning of transverse section. The resulting relative solubility ratios of  $P_{ma}/P_{ws}$  plotted in Fig. 5d, can be used to evaluate the solid solubility of Cu in the  $\alpha$ -Al matrix. An average value of this  $P_{ma}/P_{ws}$  ratio for Up-TMF processing was 0.377, compared to 0.508 for No-TMF processing and 0.574 for Down-TMF processing. These results again confirm that Down-TMF processing has a marked effect on improving the solid solubility of Cu in the  $\alpha$ -Al matrix, which in turn leads to a decrease in the precipitates along the grain boundaries of the  $\alpha$ -Al phase. However, the use of Up-TMF processing tends to counter this effect.

### 3.2. Evolution of the $\alpha$ -Al matrix phase

With respect to the evolutions of the  $\alpha$ -Al matrix phase, we focused on the dendrite sizes, the primary dendrite arm spacing (PDAS), and their growth direction. The PDAS in  $\alpha$ -Al were measured on transverse sections of samples along the tangential ( $p_1$ ), diagonal ( $p_2$ ) and radial ( $p_3$ ) directions respectively, as shown in Fig. 6a; and the corresponding average values from multiple sets of measurements are presented in Fig. 6b. The results demonstrate that Down-TMF processing can effectively reduce the PDAS by a maximum of 31 % in all directions, when compared to the No-TMF processing. In contrast, Up-TMF processing leads to an overall increase of the PDAS. Similarly, these results are also evident in Fig. 2. Corresponding dendrite sizes based on EBSD results, displayed in Fig. 6c and d, show that the average sizes of the dendrites in the  $\alpha$ -Al are decreased with Down-TMF processing, compared to No-TMF processing; conversely, dendrite sizes are increased with Up-TMF processing (Fig. 6c).

From the EBSD analysis, we also find that the deviation angles for the growth direction of  $\alpha$ -Al from the direction of temperature gradient during the solidification (Fig. 6d) are reduced with Up-TMF and Down-TMF processing in comparison to the large deviation angles found in No-TMF processing. Specifically, Down-TMF processing can effectively eliminate this deviation and promote the growth of the  $\alpha$ -Al phase in the direction of temperature gradient, whereas Up-TMF processing causes a deviation with a certain angles from this direction. To illustrate this phenomenon, further EBSD statistical results shown in Fig. 7 indicate that with Up-TMF or No-TMF processing, the formation of secondary  $\alpha$ -Al dendrites are largely increased, but with Down-TMF processing they are decreased (Fig. 7a1, b1 and c1). However, without TMF,  $\alpha$ -Al dendrites with a volume fraction of about 60 % form in chaotic growth directions due to the disordered distribution of temperature and solute in the alloy melt during solidification (Fig. 7b2 and b3). By comparison, when TMF are applied during solidification, all the crystal orientations of the  $\alpha$ -Al phase become relatively in order (Fig. 7a2 and a3). However, Up-TMF processing can cause the  $\alpha$ -Al phase growing in the  $\langle 001 \rangle$  crystal orientation to deflect for a certain angle, due to the disturbance of heat flows. Conversely, under the same conditions, Down-TMF processing facilitates all the

growth of  $\alpha$ -Al along the  $\langle 001 \rangle$  crystal orientation (Fig. 7c2 and c3). Additionally, it also can be demonstrated from Figs. 2 and 3 that Down-TMF effectively promotes the  $\langle 001 \rangle$  directional growth of  $\alpha$ -Al during the sequential solidification process, eliminates secondary dendrites, refines the primary dendrites and the PDAS, as well as diminishes the generation of precipitates to improve the uniformity of the microstructure. The effects of Up-TMF processing are almost exactly the opposite.

### 3.3. Variations in mechanical properties of alloys

It is well known that there is a strong relationship between mechanical performance and microstructure [41,45,46]. So we measured the mechanical properties, including tensile strength and hardness, and analyzed the fracture surface behavior of samples. The results are shown in Fig. 8. It can be observed that Down-TMF can effectively improve the ultimate tensile strength, yield strength and elongation from 196.2 MPa, 101.2 MPa and 14.5 % in the process without TMF to 224.1 MPa, 114.5 MPa and 17.1 %; meanwhile the hardness is increased from 85.1 kg mm<sup>-2</sup> (No-TMF) to 102.1 kg mm<sup>-2</sup>. While the Up-TMF have little impacts on the tensile strength (Fig. 8a and b), but decrease the hardness to 80.2 kg mm<sup>-2</sup>. In addition, the Fig. 8 shows that with respect to all the three alloys under different process, the modes of fracture in the sequential solidification are mainly ductile due to the high elongation and the appearance of dimples. However, the growth of microstructures and the distributions of precipitates are different in the three alloys, resulting in the strength of ductility varies. Specifically, it can be demonstrated that without TMF process, the quantity and the size of dimples are small, and the dimples are not evenly distributed; resulting in a significant reduction of ductility in the mode of fracture (Fig. 8c). While, the scanning fractograph in Fig. 8d reveals that the Up-TMF has little effects on the fracture surface behavior, as well as the performance. In addition, the aggregations of precipitated phases appear in the fracture surface, leading to a decrease of mechanical properties for the alloys (red squares in Fig. 8c and d). Nevertheless, the Down-TMF can effectively improve the appearance of dimples, which are connected with each other by the tear ridges and distributed uniformly (Fig. 8e). In this case, the quantity and the size of dimples containing a deeper shape are large; furthermore, the precipitated phases are distributed evenly. Ultimately, microstructural optimization and performance improvement can be obtained by the Down-TMF process.

## 4. Discussion

### 4.1. Simulation of travelling magnetic fields coupling with flow fields in the alloy melt

We coupled the magnetic fields with the flow fields in the alloy melt during solidification by the combination of Ansoft-Maxwell software and Ansoft-CFX software. Due to the strong spatial and temporal dependence of TMF [31], we used the effective electric current  $I_e$  (17A) to represent the strength of the magnetic fields. In addition, the distribution of magnetic fields in the alloy melt was characterized by the average magnetic force density of each position over a certain period. Furthermore, all the values of magnetic force density were imported into Ansoft-CFX with the same alloy melt model to conduct the coupling calculations of flow fields and magnetic fields. The distributions of the temperature and melt flows during solidification process were simulated (images of the simulated results from 0 s to 0.6 s, before the melt flows reach stability, were taken), together with calculations of the flow velocities in three directions at 0.6 s; and the results are shown in Figs. 9–11. Firstly, with respect to the shape of solid-liquid interfaces from 0 s

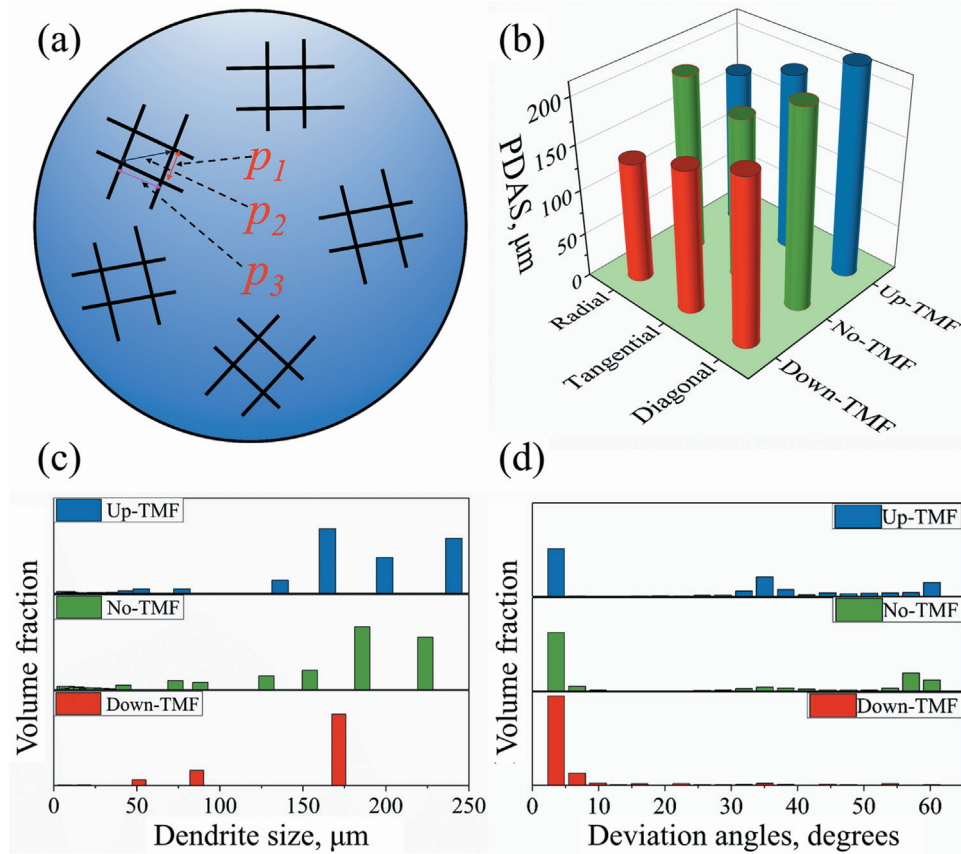


**Fig. 6.** Related statistical results of the as-cast microstructural morphologies. (a) The measuring method used to calculate the PDAS using Image-Pro software. The  $p_1$ ,  $p_2$  and  $p_3$  in (a) denote the PDAS value in the tangential, diagonal and radial directions, respectively. (b) Results of the measurements of the PDAS. (c) The dendrite sizes in the  $\alpha$ -Al phase, as measured by EBSD. (d) Deviation angles for the growth direction of  $\alpha$ -Al in the direction of temperature gradient, again measured by EBSD.

to 0.6 s; a slight concave nature was noted with No-TMF processing near the mushy zone (Fig. 9). This follows as the latent heat generated at the solidification front causes the temperature to be higher at the center of the melt than at the sidewalls where the cooling rates are faster. Additionally, slow, short-range, upward (Area A in Fig. 9) and downward (Area B) flows appear in front of the mushy zones along the direction of the temperature gradient, again resulting in a non-uniform distributions of temperature. Indeed, we find that TMF can produce long-range directional circular flows to directly alter the shape of the solid-liquid interface (Figs. 10 and 11). Specifically, with Up-TMF processing, long-range, rapid downward flows (Flow 1 in Fig. 10) appear in the center of the melt, which inhibit the transport of latent heat at the solidification front. Conversely, long-range, rapid upward flows (Flow 3) appear near the sidewalls of the melt, which can accelerate the transfer of latent heat. As a result, the temperature at the center of the melt is about 50 K higher than at the sidewalls at the same level, which induces the intense concave solid-liquid interface in the mushy zone (Fig. 10). A further factor is that the slow radial flows (Flow 2 in Fig. 10) transport the higher temperature melt from the center to the sidewalls, which causes a temperature gradient to form at the solid-liquid interface. Ultimately, the long-range directional circular flows produced by Up-TMF, consisting of Flow 1, Flow 2 and Flow 3, can radically affect the distribution of temperature in the alloy melt (Fig. 10). Conversely, in the Down-TMF process, long-range, rapid upward flows (Flow 4) appear in the center of melt at the solidification front, while long-range, rapid downward flows (Flow 6) appear near the sidewalls of the melt. Similarly, the slow radial flows (Flow 5) induce a decrease in temperature of the melt from the sidewalls to the center (Fig. 11). In this case, the long-range

directional circular flows caused by Down-TMF, consisting of Flow 4, Flow 5 and Flow 6, will also affect the distribution of temperature in the alloy melt (Fig. 11). However, the directions of the circular flows in Down-TMF processing are opposite to those in Up-TMF processing; as a result, the solid-liquid interface become convex or flat with Down-TMF processing, as seen in the mushy zone in Fig. 11. It is clear that these variations in the solid-liquid interface caused by TMF can directly change the distribution of temperature as well as the evolution of the microstructure in the alloy melt [29,30]. Accordingly, we propose three hypothetical mechanisms for this behavior.

#### 4.2. First hypothetical mechanism: mechanical stirring

To date, many literatures have attributed the dendritic refinement to the mechanical stirring caused by the magnetic fields [47–49]. The consensus is that with TMF processing, quantities of refined grains and dendrites appear in the microstructure, resulting in a consequent decrease in PDAS. Nevertheless, this mechanism is mainly applicable to the conditions that the melt flow velocities are larger than the critical large Reynolds number  $Re_{cr}$  (2300) and the critical magnetic Taylor number  $Ta_{m,cr}$  ( $1.23e+5$ ) [50–52]. Therefore, we calculated the results by using the following relationships [50–52]:

$$Re = 2\rho v_r r / \eta, \quad (4)$$

$$Ta_m = B^2 r^4 \sigma \pi f / \rho \eta^2, \quad (5)$$

where  $Re$  is the maximum Reynolds number,  $\rho$  is the density of Al-5 wt.%Cu alloy which varies with the melt temperature  $T$ ,  $v_r$  is the

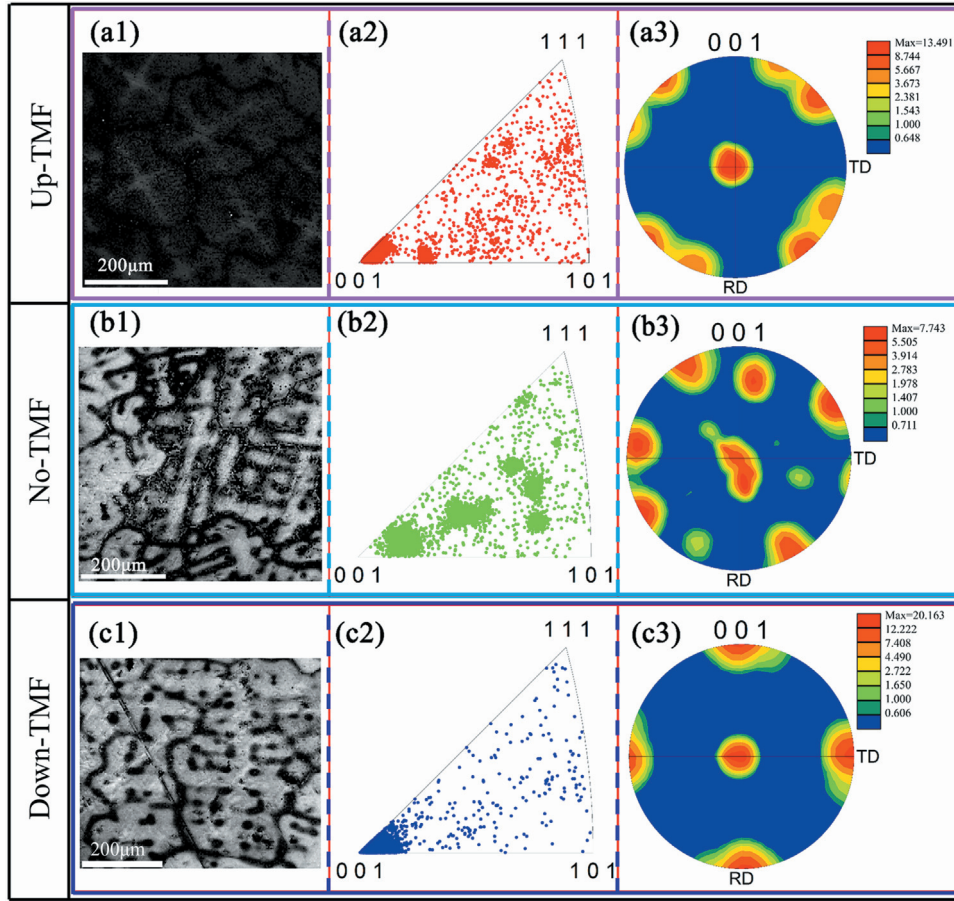


**Fig. 7.** Statistical results of the crystal orientation measurements of the  $\alpha$ -Al phase determined by EBSD. The “a”, “b” and “c” stand for the results of Up-TMF, No-TMF and Down-TMF respectively. The numbers “1”, “2” and “3” denote the serial number of photos. (a1), (b1), and (c1) are the IQ images of EBSD maps. (a2), (b2), and (c2) are the corresponding  $\langle 001 \rangle$ -inverse pole figures. (a3), (b3), and (c3) are the corresponding  $\langle 001 \rangle$ -pole figures.

maximum velocity of the melt flow,  $\eta$  is the viscosity coefficient,  $Ta_m$  is the magnetic Taylor number,  $B$  is the magnetic field intensity,  $r$  is the sample radius,  $\sigma$  is the electrical conductivity of the melt, and  $f$  is the current frequency. From the results, we obtain that the maximum Reynolds number ( $Re$ ) of the melt is 18.20 (for No-TMF), 92.04 (for Up-TMF) and 114.21 (for Down-TMF), and the magnetic Taylor number ( $Ta_m$ ) is 5.21 when TMF is applied. These values of  $Re$  and  $Ta_m$  are much lower than the theoretical critical values of  $Re_{cr}$  (2300) and  $Ta_{m,cr}$  ( $1.23e+5$ ). Consequently, the melt flows are all laminar rather than turbulent flows, which can hardly break up the dendrites. In addition, this explanation does not take into account the importance of the direction of TMF. Therefore, it is clearly inappropriate to simply attribute grain refinement to the mechanical stirring generated by TMF; accordingly, we need to seek an alternative explanation.

#### 4.3. Second hypothetical mechanism: Variation in Gibbs free energy

According to the classical theory of thermodynamics, changes in the Gibbs free energy are the driving force for the nucleation of a crystal, whereas variations in interfacial free energy provide the resistance to this nucleation [47]. The changes in Gibbs free energy for the growth of primary  $\alpha$ -Al dendrite can be written as:

$$\Delta G_g = \tau \cdot S_g + V \cdot \Delta G_V, \quad (6)$$

where  $\Delta G_g$ ,  $\tau$  and  $\Delta G_V$  respectively denote the changes in Gibbs free energy, interfacial free energy and volume free energy for the

solid-liquid phase transformation.  $S_g$  denotes the superficial area of crystal nucleus, and  $V$  denotes the volume of the crystal nucleus. Accordingly, Eq. (6) can be written in terms of the radius  $R$  of the nucleated crystal as:

$$\Delta G_g = \tau \cdot 4\pi R^2 + (4/3) \pi R^3 \cdot \Delta G_V, \quad (7)$$

where the critical nucleation radius  $R_c$  can be obtained from:

$$R_c = -2\tau / \Delta G_V. \quad (8)$$

When the TMF processing is added, the Gibbs free energy changes induced by the extra energy are introduced into the alloy melt [53–55]. Therefore, Eqs. (6) and (8) can be rewritten as:

$$\Delta G_g = \tau \cdot S_g + V \cdot \Delta G_V + V \cdot \Delta G_{TMF}, \quad (9)$$

$$R_{TMF} = -2\tau / (\Delta G_V + \Delta G_{TMF}), \quad (10)$$

where  $\Delta G_{TMF}$  is the magnetic free energy which increases with the strength of the magnetic fields [56], and  $R_{TMF}$  is the critical nucleation radius in the presence of TMF. Clearly, the value of  $R_{TMF}$  will be less than  $R_c$ . Thus, theoretically, the addition of TMF will cause a reduction in the critical nucleation radius, which is conducive to the nucleation of  $\alpha$ -Al and to reducing the grain and dendrite sizes. Similarly, this explanation fails to take into account the importance of the direction of TMF. However, our findings in this paper show that although the new free energy  $\Delta G_{TMF}$  in both cases are equal, Down-TMF is favorable for the grain refinement, while the Up-TMF does the opposite. Consequently, this hypothesis based on a perspective from Gibbs free energy cannot explain the converse results

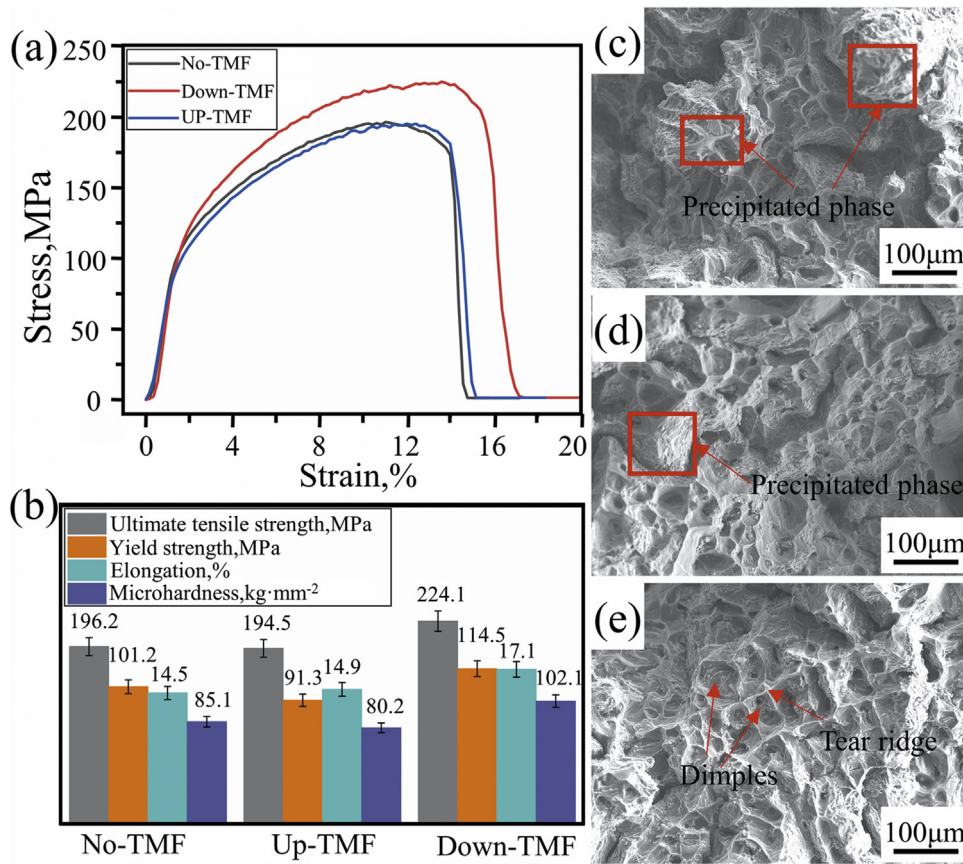


**Fig. 8.** Performance testing results. (a) Stress-strain curves. (b) Performance statistics. (c), (d) and (e) are scanning fractograph for No-TMF, Up-TMF and Down-TMF, respectively.

under different directional TMF processing. Therefore, we should propose a new viewpoint to explain the effect of TMF.

#### 4.4. Third hypothetical mechanism: Long-range directional circular flows

Based on our analysis, we propose and believe the hypothesis that the long-range directional melt flows generated by TMF to be the most likely explanation for the changes of solidification behavior, due to the mass and heat transfer produced by these flows. Specifically, long-range directional melt flows can alter the transport of the Cu solutes between high and low concentration zones, as well as the temperature distribution between high and low temperature zones in alloy melt, in turn can profoundly change the solidification paths and solutes partition coefficients [57]. Following on from this, we investigate the evolution of microstructure and solidification behavior, in both the transient and steady state during the solidification process, and show the results in Fig. 12. For the distributions of the solute at the solid-liquid interface, shown in Fig. 12c, the transient state of sequential solidification can be defined by [58]:

$$k_0 = C_S/C_L, \quad (11)$$

where the  $C_L$  and  $C_S$  are, respectively, the solute concentrations in the liquid phase and solid phase at the transient state period, and  $k_0$  is the solute partition coefficient ( $k_0 < 1$ ). In the sequential solidification process, Down-TMF can accelerate the transport of excess Cu solute, generated at the solidification front, to a distant region of the melt with a higher temperature and lower solute concentration (Fig. 11), so as to curtail the enrichment of solute. Ultimately, the instantaneous solute concentration  $C_{L-(Down-TMF)}$  in the liq-

uid phase at the solidification front will decrease, in contrast to the value of  $C_{L-(No-TMF)}$  in the process without TMF (Fig. 12c). At this point, the values of  $C_{S-(Down-TMF)}$  and  $C_{S-(No-TMF)}$  in the solid phase can be regarded as equal. Therefore, from Eq. (11), the instantaneous solute partition coefficient  $k_0-(Down-TMF)$  will be larger than  $k_0-(No-TMF)$ . Considering that the compositional undercooling may occur due to the solute enrichment at the solidification front, the transient state of sequential solidification can be evaluated by [58,59]:

$$\frac{G_T}{v_g} \leq m \frac{C_0}{D_d} \left( \frac{1 - k_0}{k_0} \right), \quad (12)$$

where the  $G_T$  is the temperature gradient of the alloy melt,  $C_0$  is the solute concentrations in the initial solution,  $m$  is the slope of liquid phase,  $v_g$  is the rate of interface movement and  $D_d$  is the diffusion coefficient of solute in liquid phase. Wherein  $C_0$ ,  $m$ ,  $v_g$  and  $D_d$  can be specified to be constant, due to the fact that the movement of the solid-liquid interface has not yet begun at a specific moment in the solidification process. In addition, compared with the solidification without TMF, the  $G_T-(Down-TMF)$  in Down-TMF processing will increase on account of the transfer of latent heat from mushy zone to the high temperature zone by long-range directional circular flows. On the contrary, the  $G_T-(Up-TMF)$  in Up-TMF processing will decrease. Here, Eq. (12) is used as the basis for judging whether compositional undercooling occurs or not [60,61]. When the inequality is true, the compositional undercooling is easy to form. Based on the results that  $k_0-(Down-TMF)$  and  $G_T-(Down-TMF)$  are larger than  $k_0-(No-TMF)$  and  $G_T-(No-TMF)$ , compositional undercooling cannot be produced with Down-TMF processing (Eq. 12). In addition, the changes in the instantaneous solute partition coefficient can also affect the instantaneous melting temperature

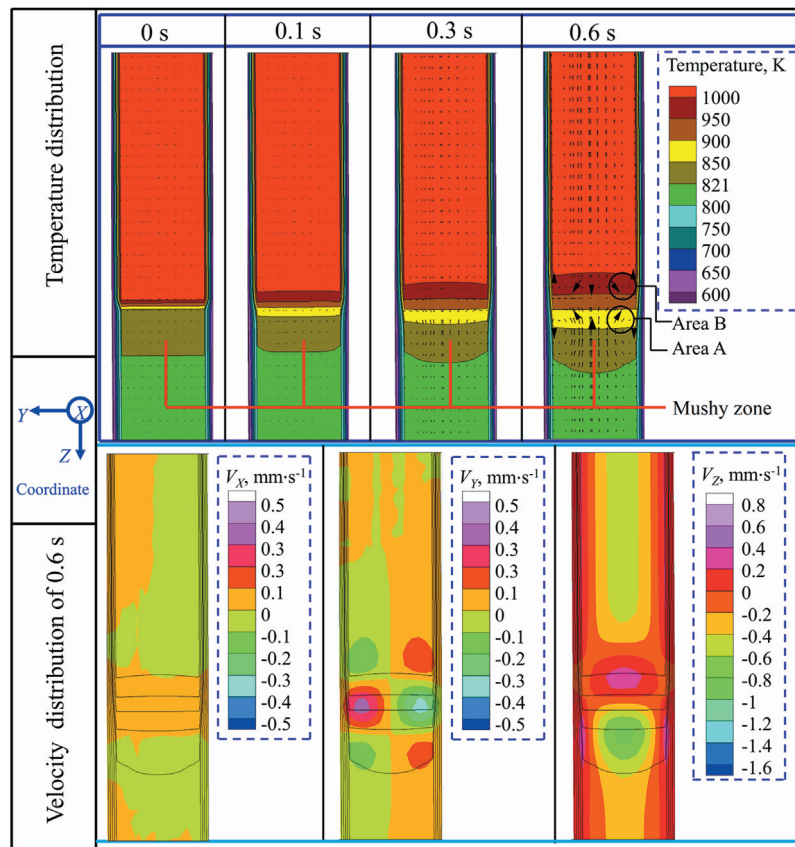


**Fig. 9.** The distribution of temperatures and melt flows at different times with the flow velocities after 0.6 s with No-TMF processing. The black arrows indicate the directions of the melt flow.

$T_L$  of the alloys in the transient state of sequential solidification, as [58,59]:

$$T_L = T_0 - mC_0 \left[ 1 + \frac{1 - k_0}{k_0} \exp\left(-\frac{v_g N}{D_d}\right) \right], \quad (13)$$

where  $T_0$  is the melting temperature of the pure solvent,  $T_L$  is the instantaneous melting temperature of the alloy in the transient state of sequential solidification, and  $N$  is the position of solid-liquid interface. From Eq. (13), due to the increase of instantaneous solute partition coefficient  $k_0$ , the value of the momentary melting temperature  $T_L$ -(Down-TMF) at the solidification front will be higher than  $T_L$ -(No-TMF), as shown in Fig. 12c. Moreover, from Fig. 11, Down-TMF can effectively transfer the latent heat from the solid-liquid interface to the distant melt, resulting in a rapid cooling at the solidification front. In addition,  $T_L$ -(Down-TMF) and undercooling temperature  $\Delta T_k$ -(Down-TMF) at the solidification front can be increased. As a result, the adsorption of Cu atoms in the  $\alpha$ -Al matrix phase, the lattice matching and the solid solubility of Cu in matrix phase  $\alpha$ -Al will all be indirectly improved [58,59].

In summary, Down-TMF can increase the instantaneous solute partition coefficient  $k_0$ , which can inhibit the appearance of compositional undercooling and reduce the solute concentrations  $C_L$  in the liquid phase at the solidification front. As a result, the aggregation and growth of the precipitate phases, including  $\text{Al}_2\text{Cu}$ ,  $\text{AlCu}$  and  $\text{AlCu}_3$ , are inhibited. Furthermore, Down-TMF can increase the momentary melting temperature  $T_L$  and promote the transfer of latent heat from the solid-liquid interface to the distant melt, resulting in an increase of the undercooling temperature  $\Delta T_k$ ; in turn, to improve the solid solubility of Cu in matrix  $\alpha$ -Al phase. Conversely, Up-TMF will produce opposite effects in the directional transport of solute and heat. Specifically,  $C_L$ -(Up-TMF) will be increased,  $T_L$ -(Up-TMF),  $\Delta T_k$ -(Up-TMF) and  $k_0$ -(No-TMF) will be

decreased, and compositional undercooling will be produced at the solidification front. As a result, the precipitate phases can aggregate easily along grain boundaries and the solid solubility of Cu in the matrix  $\alpha$ -Al phase will decrease accordingly.

By using the Lever-rule model and the Scheil model [58,59], the solidification paths for sequential solidification at steady-state were calculated by the Pandat software. In addition, the results in Fig. 12a show that the solidification temperature is 840 K based on the Lever-rule model, and 821 K based on the Scheil model. In this paper, we first used the Scheil model to simulate the solidification process under an ideal condition, that is, the infinite diffusion in liquid phase and no diffusion in solid phase. However, when calculating the actual experiments, we only referred to the non-diffusion behavior in solid phase according to the Scheil model. In this case, the effects of “No-TMF”, “Up-TMF” and “Down-TMF” on liquid phase diffusion and a series of results were studied. Therefore, the phase diagram curves under the ideal condition calculated by the Scheil model can be shown as the solid black lines in Fig. 12b. During the actual sequential solidification without TMF, weak flows, generated by gravity, buoyancy and heat transfer (Area B of Fig. 9), will limit the solute diffusion at the solidification front, which can cause the solute concentration  $C_L$ -(No-TMF) in the liquid phase at steady-state to increase. In addition, from the principle of mass conservation,  $C_S$ -(No-TMF) will also decrease at steady-state. Accordingly, the phase diagram curves without TMF are approximated as Lines 1 in Fig. 12b, for the sequential solidification process. Therefore, by comparison to the case of the Scheil model, the solidification intervals  $\Delta T_0$ -(No-TMF) during sequential solidification are increased, whereas the solute distribution coefficient  $k_0$ -(No-TMF) at steady-state decreases. While, because of the long-range directional circular flows generated in

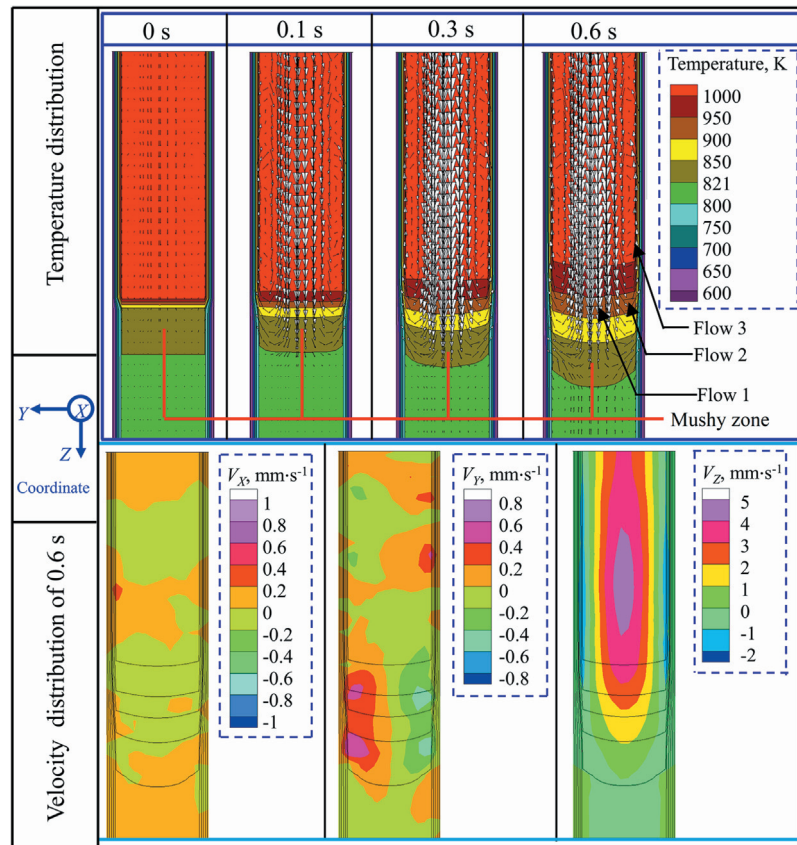


**Fig. 10.** The distribution of temperature and melt flows at different times with the flow velocities after 0.6 s with Up-TMF processing. The white arrows indicate the directions of the melt flow.

Down-TMF processing (Fig. 11), the transport of excess solute from the solidification front to the distant melt, will be greatly enhanced. Under these circumstances, the solute concentration  $C_L'$ -(Down-TMF) in liquid phase at steady-state become less than  $C_L'$ -(No-TMF); accordingly, the  $C_S'$ -(Down-TMF) will be larger than the  $C_S'$ -(No-TMF), such that the curves on the phase diagram under Down-TMF process will shift to the solid pink Lines 3 in Fig. 12b. Similarly, we find that the solidification intervals  $\Delta T_0$ -(Down-TMF) will be less than  $\Delta T_0$ -(No-TMF), while the value of solute distribution coefficient  $k_0'$ -(Down-TMF) at steady-state during sequential solidification will become larger than  $k_0'$ -(No-TMF). However, the long-range directional circular flows induced by Up-TMF (Fig. 10) will rapidly transfer the solute from distant regions of the melt to the solidification front to enhance the solute enrichment at the solid-liquid interface. Furthermore, the solute concentration  $C_L'$ -(Up-TMF) in the liquid phase at steady-state will become larger than  $C_L'$ -(No-TMF); nevertheless,  $C_S'$ -(Up-TMF) will be less than  $C_S'$ -(No-TMF). As a result, the phase diagram curves after Up-TMF processing change into the blue dotted Lines 2 in Fig. 12b. Likewise, we find that the solidification intervals  $\Delta T_0$ -(Up-TMF) are larger than  $\Delta T_0$ -(No-TMF), while the  $k_0'$ -(Up-TMF) at steady-state becomes less than  $k_0'$ -(No-TMF). It is well known that the changes in the solidification intervals  $\Delta T_0$ , the solute distribution coefficient  $k_0$ , the undercooling temperature  $\Delta T_k$  and the momentary melting temperature  $T_L$  can effectively alter the solidification behavior, ultimately leading to corresponding evolutions in the microstructural morphology and the precipitated phases in the alloys [62]. Consequently, we believe that this hypothesis of long-range directional forced melt flows is most reasonable to explain the specific effects of TMF on microstructure evolutions in alloys with large solidification intervals. Hence, we provide a detailed elucidation

of this mechanism below by combining the relationship between microstructure and mechanical performance.

#### 4.5. Deterministic mechanism of TMF on the microstructure and performance

Using the schematic illustration in Fig. 13, we can describe mechanistically how the coupling of TMF with sequential solidification can markedly alter solidification behavior and hence affect the microstructural evolution and performance of cast Al-5 wt.%Cu alloys. The specific mechanisms primarily involve the transmission and redistribution of solute and temperature, which can be attributed to the long-range directional circular flows induced by TMF. Firstly, as shown in Fig. 13a, two opposite directional melt flows, induced by gravity, buoyancy and heat exchange, appear at the solidification front with No-TMF processing. Along the direction of temperature gradient, melt flows below can enhance the transport of solute and latent heat to the regions of the melt distant from the center, which serves to promote the growth of primary dendrites. However, the above melt flows inhibit these events. Consequently, the primary  $\alpha$ -Al dendrites grow in a deflected manner toward the center of the melt and significant secondary dendrites are formed, due to the inhibition of mass and heat transfer. However, such inhibitions are eliminated with Down-TMF processing, because of the fast transmission of solute and latent heat from the solidification front to the distant regions of the melt (Fig. 13b). This is equivalent to increasing the degree of temperature undercooling, while inhibiting the compositional undercooling [63]. Therefore, the growth of the  $\langle 001 \rangle$  primary  $\alpha$ -Al dendrites is greatly increased, while the growth of the secondary dendrites is severely suppressed. Combined with the results in Eqs. (11)–(13), the values of the

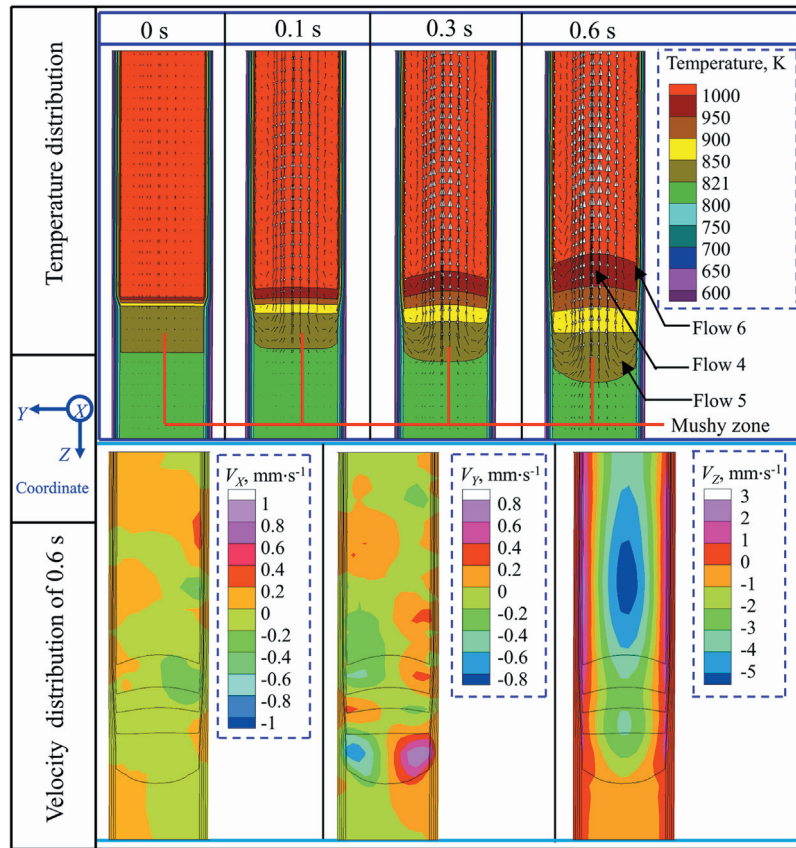


Fig. 11. The distribution of temperatures and melt flow at different times with the flow velocities after 0.6 s with Down-TMF processing. The white arrows indicate the directions of the melt flows.

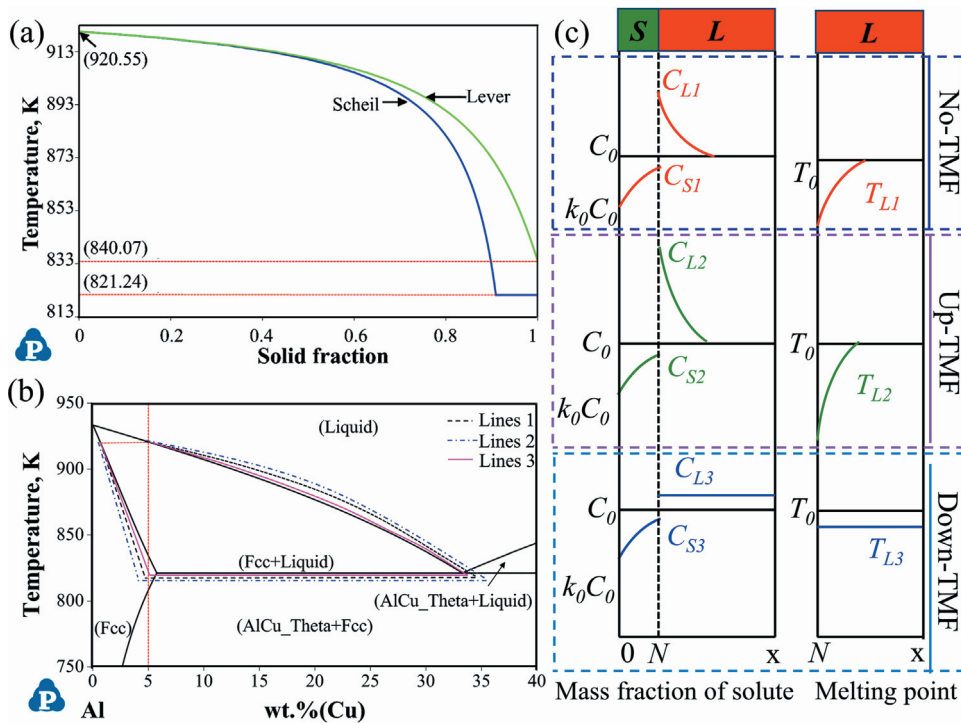
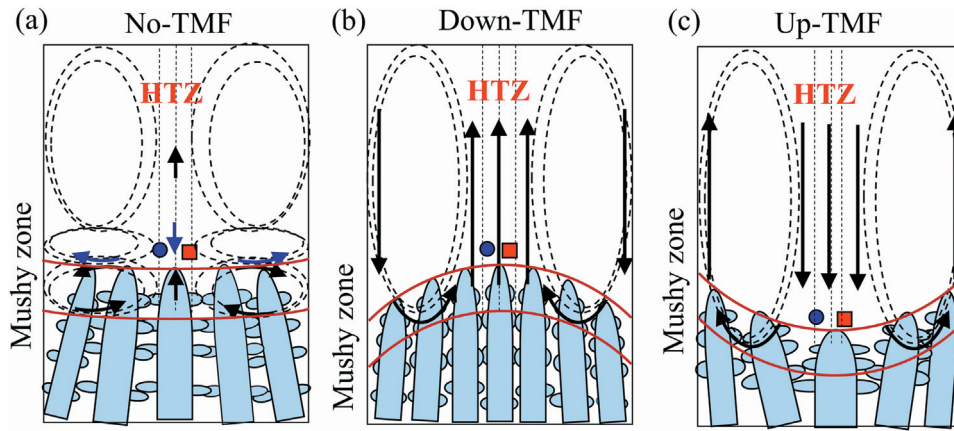


Fig. 12. Schematic diagrams of solidification process under different conditions. (a) Solidification path models. (b) Phase diagram curves. Lines 1, Lines 2 and Lines 3 in (b) are the equivalent phase diagram curves of No-TMF, Up-TMF and Down-TMF, respectively. (c) Distributions of solutes and temperatures at the solid-liquid interface. In (c), S refers to solid phase, L refers to liquid phase, T is the melting point, N is the position of solid-liquid interface, x is the position of the alloy melt distant from the solid-liquid interface and  $C_0$ ,  $C_L$ , and  $C_S$  are, respectively, the solute concentration of the initial, liquid and solid states.



**Fig. 13.** Schematic diagrams showing the mechanisms for different TMF processes coupled with sequential solidification. The purple circles are the solute enriched at the solidification front. The red squares are the latent heat generated at the solidification front. "HTZ" denotes a higher temperature zone. The purple and black arrows in (a) (b) and (c) represent melt flows.

solute distribution coefficient  $k_0$ , the undercooling temperature  $\Delta T_k$  and the momentary melting temperature  $T_L$  are all increased by Down-TMF processing, whereas the solidification interval  $\Delta T_0$  is decreased. We can evaluate the growth of the solid-liquid interface by using [64–66]:

$$v_g = G_T D_d / \Delta T_0, \quad (14)$$

$$\lambda_1 = 4.3 \left( \frac{\Delta T_0 D_d \Gamma}{k_0} \right)^{\frac{1}{4}} G_T^{-\frac{1}{2}} \cdot v_g^{-\frac{1}{4}}, \quad (15)$$

$$\lambda_2 = 7.5 t_1^{0.39}, \quad (16)$$

where  $v_g$  is the velocity of stable growth for the flat interface,  $\lambda_1$  and  $\lambda_2$  are the PDAS and secondary dendritic arm spacing, respectively,  $\Gamma$  is the Gibbs-Thomson coefficient, and  $t_1$  is the local solidification time at solid-liquid interface. From Eqs. (14)–(16), it can be deduced that Down-TMF processing causes both  $\lambda_1$  and  $\lambda_2$  to be decreased. Moreover, the solid solubility of Cu in the  $\alpha$ -Al matrix is also raised due to the increasing values of  $k_0'$  and  $C_5'$  (Down-TMF) at steady-state during sequential solidification; leading to a reduction in other precipitated phases. Correspondingly, the size of  $\alpha$ -Al dendrites and the PDAS are both decreased as the microstructure becomes more uniform; meanwhile the quantity of precipitated phases is reduced, while the solid solubility of Cu in the  $\alpha$ -Al matrix is increased. Therefore, the hardness of the matrix will increase significantly [67]. In regard to the tensile strength, due to the decrease of PDAS and secondary dendritic arm spacing, as well as the increase of uniformly distributed matrix phases growing along the temperature gradient caused by Down-TMF, the tensile stress and the numerous large and deep dimples can be more uniform, in turn, to increase the ultimate tensile strength, yield strength, elongation and ductility of alloys [45,46]. In addition, Down-TMF effectively decrease the volume fraction of precipitated phases, so as to largely improve the ductility of alloys [41]. In comparison to Down-TMF processing, Up-TMF processing will generate long-range circular flows in opposite directions (Fig. 13c), which will restrain the axial transmission of the excess solutes and latent heat from solidification front to the distant regions of the melt. Eventually, the solute will accumulate at the solid-liquid interface and lead to severe compositional undercooling. In addition, the latent heat cannot be dissipated along the axial direction, which results in a more intense increase of temperature at the solidification front, as well as the serious inhibition to the growth of primary  $\alpha$ -Al dendrites. However, radial heat dissipation is enhanced, which can improve the growth of secondary dendrites and severe deflections in the growth directions of the primary dendrites. Eventually

Up-TMF can increase the dendrite sizes, the PDAS and precipitate content. Moreover Up-TMF can generate the inhibitions of the growth of primary dendrites, promote the growth of secondary dendrite, and decrease the solid solubility of Cu in the  $\alpha$ -Al matrix. Therefore, Up-TMF have the negative effects on mechanical performance of alloys, in particular, it may lead to a significant reduction of ductility in the mode of fracture.

## 5. Conclusions

- (1) By coupling the TMF with sequential solidification, the mushy zones of Al-Cu-based alloys with large solidification intervals can be continuously regulated, further to modify the microstructures and mechanical properties, due to the long-range directional circular flows generated by TMF.
- (2) Only the Down-TMF can lead to an equivalent increase in the solute partition coefficient. Furthermore, the process causes reductions in the solidification intervals, the grain and dendrite sizes, the PDAS and precipitate content; moreover, it enhances the quantity of primary  $\alpha$ -Al dendrites growing along the direction of temperature gradient and the solid solubility of Cu in this phase. That is, Down-TMF is the preferred process to acquire refined and homogeneous microstructures. Conversely, Up-TMF results in a series of opposite and less desirable effects on the solidification behavior and microstructures.
- (3) Only the Down-TMF can significantly enhance the mechanical properties, including the ultimate tensile strength, yield strength, elongation and hardness, as well as make the fracture mode ductile; however, Up-TMF reduces the performance and ductility of alloys.

## Acknowledgements

This work was supported by the National Key Research and Development Program of China [2017YFA0403804] and National Natural Science Foundation of China [51425402, 51671073].

## References

- [1] W.W. Mullins, R. Sekerka, *J. Appl. Phys.* 35 (1964) 444–451.
- [2] J.M. Rosalie, L. Bourgeois, *Acta Mater.* 60 (2012) 6033–6041.
- [3] L. Gao, X. Ou, S. Ni, K. Li, Y. Du, M. Song, *Mater. Sci. Eng., A* 762 (2019), 138091.
- [4] G. Liu, J. Sun, C.-W. Nan, K.-H. Chen, *Acta Mater.* 53 (2005) 3459–3468.
- [5] J. Rutter, B. Chalmers, *Can. J. Phys.* 31 (1953) 15–39.
- [6] W. Tiller, K. Jackson, J. Rutter, B. Chalmers, *Acta Metall.* 1 (1953) 428–437.
- [7] Z. Gao, W. Jie, Y. Liu, H. Luo, *Acta Mater.* 127 (2017) 277–286.
- [8] P. Lee, J. Hunt, *Acta Mater.* 49 (2001) 1383–1398.

- [9] I. Ferreira, C. Siqueira, C. Santos, A. Garcia, *Scr. Mater.* 49 (2003) 339–344.
- [10] H. Elhadari, H. Patel, D. Chen, W. Kasprzak, *Mater. Sci. Eng., A* 528 (2011) 8128–8138.
- [11] E.E. Obaldia, S. Felicelli, *J. Mater. Process. Technol.* 191 (2007) 265–269.
- [12] D.A. Lados, D. Apelian, *Mater. Sci. Eng., A* 385 (2004) 200–211.
- [13] H. Meidani, J.L. Desbiolles, A. Jacot, M. Rappaz, *Acta Mater.* 60 (2012) 2518–2527.
- [14] J. Delahaye, J.T. Tchuindjang, J. Lecomte-Beckers, O. Rigo, A. Habraken, A. Mertens, *Acta Mater.* 175 (2019) 160–170.
- [15] H. Neumann-Heyme, K. Eckert, C. Beckermann, *Acta Mater.* 140 (2017) 87–96.
- [16] J.A. Spittle, *Int. J. Cast Met. Res.* 19 (2006) 210–222.
- [17] X. Li, Q. Cai, B. Zhao, Y. Xiao, B. Li, *J. Alloys Compd.* 675 (2016) 201–210.
- [18] H. Liu, Y. Gao, L. Qi, Y. Wang, J.F. Nie, *Metall. Mater. Trans. A* 46 (2015) 3287–3301.
- [19] D.V. Alexandrov, P.K. Galenko, *Phys. Usp.* 57 (2014) 771.
- [20] S. Liu, D. Zhang, J. Xiong, C. Chen, T. Song, L. Liu, S. Huang, *J. Alloys Compd.* 781 (2019) 873–882.
- [21] X. Zhang, L. Huang, B. Zhang, Y. Chen, S. Duan, G. Liu, C. Yang, F. Liu, *Mater. Sci. Eng. A* 753 (2019) 168–178.
- [22] J. Gao, M. Han, A. Kao, K. Pericleous, D.V. Alexandrov, P.K. Galenko, *Acta Mater.* 103 (2016) 184–191.
- [23] H. Wei, F. Xia, S. Qian, M. Wang, *J. Mater. Process. Technol.* 240 (2017) 344–353.
- [24] F. Wang, D. Eskin, J. Mi, C. Wang, B. Koe, A. King, C. Reinhard, T. Connolley, *Acta Mater.* 141 (2017) 142–153.
- [25] C. Lin, S. Wu, S. Lü, P. An, L. Wan, *J. Alloys Compd.* 568 (2013) 42–48.
- [26] M.H. Avnaim, B. Mikhailovich, A. Azulay, A. Levy, *Int. J. Heat Fluid Flow* 69 (2018) 9–22.
- [27] K. Zhang, Y. Li, Y. Yang, *J. Mater. Sci. Technol.* 48 (2020) 9–17.
- [28] Y. Zhao, K. Wang, S. Yuan, Y. Ma, G. Li, Q. Wang, *J. Mater. Sci. Technol.* 46 (2020) 127–135.
- [29] E. Liotti, A. Lui, S. Kumar, Z. Guo, C. Bi, T. Connolley, P. Grant, *Acta Mater.* 121 (2016) 384–395.
- [30] R. Mathiesen, L. Arnberg, P. Bleuet, A. Somogyi, *Metall. Mater. Trans. A* 37 (2006) 2515–2524.
- [31] G. Zimmermann, C. Pickmann, M. Hamacher, E. Schaberger-Zimmermann, H. Neumann-Heyme, K. Eckert, *Acta Mater.* 126 (2017) 236–250.
- [32] D. Ruvalcaba, R. Mathiesen, D. Eskin, L. Arnberg, L. Katgerman, *Acta Mater.* 55 (2007) 4287–4292.
- [33] M.H. Avnaim, B. Mikhailovich, A. Azulay, A. Levy, *Int. J. Heat Fluid Flow* 69 (2018) 23–32.
- [34] K. Dadzis, G. Lukin, D. Meier, P. Bönisch, L. Sylla, O. Patzold, *J. Cryst. Growth* 445 (2016) 90–100.
- [35] Z.Y. Li, X.F. Qi, L.J. Liu, G.S. Zhou, *J. Cryst. Growth* 484 (2018) 78–85.
- [36] P. Schwesig, M. Hainke, J. Friedrich, G. Mueller, *J. Cryst. Growth* 266 (2004) 224–228.
- [37] H. Yan, T. Gao, H. Zhang, J. Nie, X. Liu, *J. Mater. Sci. Technol.* 35 (2019) 374–382.
- [38] X. Yang, J. Zhu, W. Li, *J. Mater. Sci. Technol.* 31 (2015) 1320–1328.
- [39] B. Lin, R. Xu, H. Li, W. Zhang, *J. Mater. Sci. Technol.* 34 (2018) 1447–1459.
- [40] Y. Kaygisiz, N. Marasli, *J. Alloys Compd.* 721 (2017) 764–771.
- [41] E. Cadirli, *Met. Mater. Int.* 19 (2013) 411–422.
- [42] S. Xi, K. Zuo, X. Li, G. Ran, J. Zhou, *Acta Mater.* 56 (2008) 6050–6060.
- [43] H. Lipson, *Contemp. Phys.* 20 (1979) 87–88.
- [44] P.T. Dawson, S.A. Petrone, *Surf. Sci.* 152 (1985) 925–931.
- [45] N.J. Petch, *J. Iron Steel Inst.* 174 (1953) 25–28.
- [46] E.O. Hall, *Proc. Phys. Soc. B* 64 (1951) 747.
- [47] C.J. Li, Z.M. Ren, W.L. Ren, Y.Q. Wu, *Trans. Nonferrous Met. Soc. China* 22 (2012) s1–s6.
- [48] X. Li, A. Gagnoud, Y. Fautrelle, Z. Ren, R. Moreau, Y. Zhang, C. Esling, *Acta Mater.* 60 (2012) 3321–3332.
- [49] E. Liotti, A. Lui, S. Kumar, Z. Guo, C. Bi, T. Connolley, P.S. Grant, *Acta Mater.* 121 (2016) 384–395.
- [50] A. Noeppel, A. Ciobanas, X.D. Wang, K. Zaidat, N. Mangelinck, O. Budenkova, A. Weiss, G. Zimmermann, Y. Fautrelle, *Metall. Mater. Trans. B* 41 (2009) 193–208.
- [51] A.T. Richardson, *J. Fluid Mech.* 63 (2006) 593–605.
- [52] N. Rott, *Annu. Rev. Fluid Mech.* 22 (1990) 1–12.
- [53] T. Hou, Z. Li, K. Wu, H. Lin, Y. Li, G. Zhang, W. Liu, *Acta Mater.* 167 (2019) 71–79.
- [54] R. Xin, K. Wu, G. Zhang, T. Hou, G. Ma, W. Qiao, H. Zhao, *J. Mater. Sci. Technol.* 34 (2018) 786–793.
- [55] B. Dong, T. Hou, K. Wu, Z. You, Z. Li, G. Zhang, H. Lin, *Mater. Lett.* 240 (2019) 66–68.
- [56] T. Kakeshita, T. Saburi, K. Kindo, S. Endo, *J. Appl. Phys.* 36 (1997) 7083.
- [57] D. Medvedev, T. Fischaleck, K. Kassner, *J. Cryst. Growth* 303 (2007) 69–73.
- [58] Y. Xu, D. Casari, Q. Du, R.H. Mathiesen, L. Arnberg, Y. Li, *Acta Mater.* 140 (2017) 224–239.
- [59] L. Wang, W. Lu, Q. Hu, M. Xia, Y. Wang, J. Li, *Acta Mater.* 139 (2017) 75–85.
- [60] Y. Dong, S. Shuai, T. Zheng, J. Cao, C. Chen, J. Wang, Z. Ren, *J. Mater. Sci. Technol.* 39 (2020) 113–123.
- [61] Y. Zhao, B. Zhang, H. Hou, W. Chen, M. Wang, *J. Mater. Sci. Technol.* 35 (2019) 1044–1052.
- [62] P. Rudolph, *J. Cryst. Growth* 310 (2008) 1298–1306.
- [63] Y. Xu, D. Casari, R.H. Mathiesen, Y. Li, *Acta Mater.* 149 (2018) 312–325.
- [64] Y. Wang, S. Li, Z. Liu, H. Zhong, L. Xu, H. Xing, *J. Mater. Sci. Technol.* 35 (2019) 1309–1314.
- [65] Y. Zhang, X. Miao, Z. Shen, Q. Han, C. Song, Q. Zhai, *Acta Mater.* 97 (2015) 357–366.
- [66] Z. Gao, W. Jie, Y. Liu, Y. Zheng, H. Luo, *J. Alloys Compd.* 797 (2019) 514–522.
- [67] H. He, Y. Yi, S. Huang, Y. Zhang, *J. Mater. Sci. Technol.* 35 (2019) 55–63.